

Existence of three distinct scaling regimes in self-propelled rigid pitching airfoil

Rakshita Joshi^{1,2}†, and Jaywant Arakeri^{1,2}

¹Indian Institute of Science, Bangalore, India

²Indian Institute of Technology Jodhpur, India

(Received xx; revised xx; accepted xx)

Oscillating foils in self-propelled mode are the simplest model for investigating oscillatory locomotion in cruising fishes. In this investigation, we explore the self-propulsion characteristics of a NACA0015 section airfoil, with chord length C , subjected to sinusoidal pitching using a rotary apparatus. A power-spring-based crank-rocker mechanism actuates the airfoil. We examine the effect of pitching frequency (f), amplitude (A), and the pitching point location (p) on the self-propulsion speed, U_s . We present the results in terms of self-propulsion Reynolds number ($Re_s = U_s C / \nu$), reduced frequency (k_s), Strouhal number (St), and two non-dimensional speeds, U_{BL}^* (body length per oscillation) and U_{AL}^* (forward speed in terms of trailing edge excursion per oscillation). U_s increases with frequency and amplitude, but a diminishing effect of amplitude was noted at larger amplitudes. Highest speeds were achieved when pitched closest to the leading edge, with St in the range of 0.2–0.4. Three distinct scaling regimes are identified, each characterized by a specific relationship between Re_s and trailing-edge Reynolds number, $Re_{TE} = fAC/\nu$. When pitching at low-amplitude, close to leading-edge, $Re_s \sim (1-2p)Re_{TE}^{3/2}$ (*power scaling*). For higher amplitude pitching, $Re_s \sim Re_{TE}(1-2p)^{1/2}(A/C)^{-1/2}$ (*separable scaling*). When pitched close to the midpoint, the airfoil propels beyond a threshold $Re_{TE,0}$, and Re_s increases linearly with Re_{TE} (*linear scaling*). Notably, in separable and linear regimes, self-propulsion is independent of viscosity. These relations collectively offer a comprehensive framework for understanding the self-propulsion of rigid pitching airfoils across a wide range of parameters.

Key words: Swimming/flying, Self-propulsion

1. Introduction

Zoologist Gray, in an effort to determine the propulsive power of cruising dolphins (Gray 1936), stumbled upon a paradox – the drag power of the dolphins exceeds its muscle power. Although it’s now considered resolved (see, Fish & Lauder (2006) and Bale *et al.* (2015)), Gray’s paradox had long perplexed researchers studying the hydrodynamics and energetics of swimming fishes – with a singular interest in the mechanics of thrust generation and

† Email address for correspondence: rakshitaj@iisc.ac.in

swimming efficiency. The paradox revealed a fundamental aspect of fish propulsion – muscle energy is used to produce lateral undulations generating thrust, which balances the drag. Self-propulsion ensues when prescribed actuation generates sufficient thrust to overcome hydrodynamic resistance, establishing a precise balance between average thrust and drag. A body experiences a net zero force when cruising at a constant speed and is said to be “self-propelling.”

In dolphins and other oscillatory swimmers (like tuna, sharks, and trout), it is assumed that the undulations are prominent only in the posterior end of the fish, resulting in the oscillation of the caudal fin. This proposition has led to studying the propulsive characteristics of an oscillating airfoil – a model caudal fin – as an alternative to rotary propellers (Triantafyllou & Barrett 1995). Over the last four decades, a considerable body of research has delved into the propulsive characteristics of oscillating airfoils, with Wu *et al.* (2020), Smits (2019), and more recently Xing & Yang (2023) providing extensive reviews of these studies. However, the assumption that thrust results solely from caudal fin oscillations is debatable. Bainbridge (1958, 1963) observed that the caudal fin’s contribution to the total thrust varied for different fish species. Recently, Lucas *et al.* (2020) reported that the anterior body oscillations significantly contribute to thrust generation based on examination of the flow field around swimming bluegill sunfish and trout. Therefore, for understanding and designing efficient systems particularly meant for cruising over long distances, it is essential to understand the thrust-drag coupling on swimming bodies. The interplay between mechanisms that result in drag and generate thrust can significantly impact speed and efficiency.

Even oscillating airfoils exhibit a remarkable ability to self-propel when subjected to pitching, heaving, or combined pitch-heave oscillations. A few researchers have explored different aspects of self-propulsion in oscillating airfoils. See, for example, Lauder *et al.* (2007), Alben *et al.* (2012), Gazzola *et al.* (2014), Das *et al.* (2016, 2019, 2022), Lagopoulos *et al.* (2019), Liu *et al.* (2020), Wang *et al.* (2020), Gross *et al.* (2021), Paniccia *et al.* (2021), Lin *et al.* (2021) and Wu *et al.* (2022). Examining the self-propulsion of oscillating airfoils yields valuable insights into the complex hydrodynamics of fish propulsion. Subsequently, a crucial and foundational inquiry arises: what factors determine swimming speed, and how are they influenced by imposed kinematics such as frequency, amplitude, or the mode of oscillation?

The field has only recently gained attention due to the challenges posed by the experimental and numerical complexities of studying self-propulsion. The identification of spontaneous forward motion in a heaving flat plate airfoil by Vandenbergh *et al.* (2004) marks an early and systematic exploration of self-propulsion in oscillating airfoils. They noted self-propulsion beyond a critical heaving frequency, with forward speed exhibiting a linear increase with frequency beyond this point. This discovery sparked interest in examining similar phenomena in elliptical airfoils. Spagnolie *et al.* (2010) also reported a similar behaviour in their experimental and numerical study. However, numerical simulations of heaving elliptical airfoils (Alben & Shelley 2005; Zhang *et al.* 2010; Wang *et al.* 2022) revealed a non-linear relationship between self-propelling speed and heaving frequency with speed increasing as the 5/3rd power of the frequency.

Gazzola *et al.* (2014) suggest evaluating swimming behaviour by examining the correlation between the self-propulsion Reynolds number, $Re_s = U_s C / \nu$ and a trailing edge Reynolds number $Re_{TE} = f A C / \nu$ (also called the swimming number). Here, U_s , f , A , C , and ν denote the self-propulsion speed, oscillating frequency, trailing edge excursion, airfoil chord length, and the kinematic viscosity of the fluid. Gazzola *et al.* (2014) proposed a scaling law $Re_s \sim Re_{TE}^\alpha$ for macroscopic aquatic swimmers, with $\alpha = 4/3$ and 1 in laminar and turbulent flow, respectively. They arrive at these scaling relations considering a dynamical balance between inertial thrust and appropriate skin friction model. They further substantiated these

scaling relationships through 3D numerical simulations of a model carangiform swimmer and swimming data of a large taxa of fishes. [Das et al. \(2016, 2019\)](#) reported a similar power law relationship with $Re_s \sim Re_{TE}^{1.6}$ for low amplitude sinusoidal and non-sinusoidal pitching. They, however, account for enhanced skin friction drag due to boundary layer thinning in moving bodies which results in a slightly larger value of the exponent with $\alpha = 1.6$ as compared to 1.33 reported by [Gazzola et al. \(2014\)](#). However, [Das et al. \(2022\)](#) also find an amplitude-dependent Re_s – Re_{TE} relation for higher amplitudes. On the other hand, [Lin et al. \(2021\)](#) report a power law with $Re_s \sim Re_{TE}^{5/3}$ valid for small and large amplitudes but at lower Reynolds numbers. [Mackowski & Williamson \(2015\)](#) report drag-thrust transitions in pitching airfoils at a small pitching amplitude of 2° through direct force measurement with $Re_s \sim Re_{TE}^{1.65}$ in line with the power-scaling observed in other studies for small-amplitude pitching.

Despite the valuable insights gained from numerical investigations into the self-propulsion of rigid airfoils, there remains a notable scarcity of experimental findings to validate the numerical results. Furthermore, the predominant focus in all the studies is on pitching frequency and amplitude, overlooking a crucial variable: the pitching point’s location. Even in exploring the effect of amplitude, divergent findings exist across studies (mainly [Das et al. \(2022\)](#) and [Lin et al. \(2021\)](#)), creating uncertainty.

In addressing the identified research gap, our present study aims to provide a comprehensive experimental foundation on the self-propulsion of pitching airfoils. We specifically focus on the effect of the pitching point’s location along with the amplitude and frequency of pitching. We identify three distinct scaling regimes – *power*, *separable*, and *linear scaling regimes* – relating Re_s and Re_{TE} across a diverse range of imposed kinematics, highlighting the different physical effects at play. The *power-scaling regime* is similar to the relations reported by [Gazzola et al. \(2014\)](#), [Das et al. \(2016, 2019, 2022\)](#), and, [Lin et al. \(2021\)](#) while accounting for the effect of the pitching point. The *linear regime* emerges when the airfoil is pitched near its center, resembling the relationship identified by [Vandenbergh et al. \(2004\)](#). However, the novel contribution of our work lies in identifying the *separable scaling regime*. This regime highlights the non-uniform contribution of amplitude and frequency at higher amplitude pitching. These findings address critical aspects such as the optimal pitching location for maximum speed and the differential contributions of frequency and amplitude in determining propulsion characteristics.

This article is divided into distinct sections for clarity. In section 2, we offer an overview of the experimental apparatus, present details of our input parameters, and provide definitions for key terms used throughout the study. Moving to section 3, we report the measured self-propelling speed and explore the impact of imposed kinematics on actual and normalized speed. In section 4, we identify the distinct scaling regimes. We also derive the different regimes by considering a balance of the inviscid reactive thrust forces with the appropriate drag scaling depending on the nature of drag forces. Finally, section 5 serves as the conclusion, summarizing our findings and proposing avenues for future exploration.

2. Experimental Methodology

We use a *NACA0015* airfoil section with chord length $C = 38.9\text{mm}$ and span $h = 100.1\text{mm}$ as our model object. The airfoil is made with Acrylonitril Butadiene Sulphide (ABS) by vacuum casting. The density of the airfoil is 1.01g/cm^3 , nearly the same as the density of the water. Details of the airfoil fabrication process can be found in [Shinde \(2012\)](#). Three $M3 \times 20\text{mm}$ threaded holes are positioned along the chord line to allow for adjustments in the pitching point location. The airfoil can be connected to the actuating system using these threaded holes.

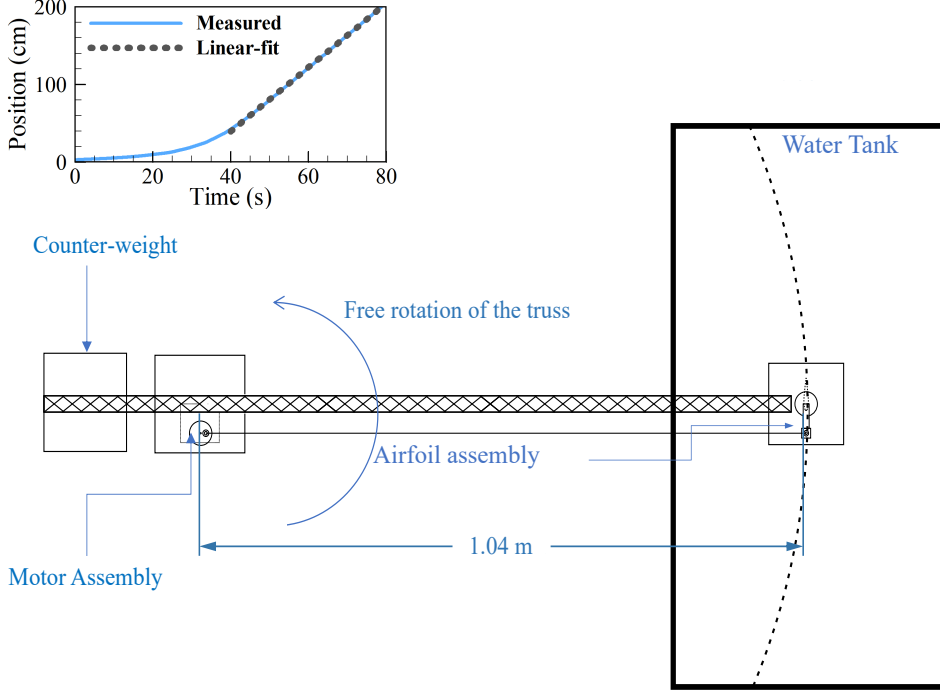


Figure 1: Schematic of the top view of the apparatus indicating the path traversed by the self-propelling airfoil. The position-time graph in the top-left corner shows the instantaneous position of the airfoil with time for with pitching at 2Hz with an amplitude of 9.5° .

We use a rotary apparatus, similar to [Thiria & Godoy-Diana \(2010\)](#), to achieve self-propulsion. Figure 1 shows the schematic of the top view of the apparatus. The airfoil is positioned at the end of a long, freely moving rotary arm with an effective length of $1.04m (> 20C)$. This configuration ensures that the airfoil's motion is nearly linear, with negligible curvature effects. The rotating arm is essentially a truss structure crafted in-house using carbon fiber for a high strength-to-mass ratio. This truss, also referred to as the rotating arm, is securely mounted on a high-precision steel shaft. The shaft is supported by a combination of axial and thrust (flat) air bearings, supporting the entire truss and the actuating system. These bearings allow free rotation of the shaft and the truss while constraining motion in other directions. Using air bearings guarantees that the frictional impact from the supporting structure is negligible compared to the forces acting on the airfoil. A spiral-spring-based crank rocker mechanism actively provides sinusoidal pitching motion to the airfoil. Further details on the apparatus construction, operation, and the mechanism's kinematics, dynamics, and characterization can be found in [Joshi & Arakeri \(2022, 2024\)](#). The airfoil can propel in a large water tank measuring $2m \times 1m \times 0.5m$. Top of the airfoil is submerged at a depth of about $5cm$ from the water surface.

We pitch the airfoil sinusoidally at a distance pC from the leading edge with frequency f and amplitude θ_0 such that the instantaneous pitch angle of the airfoil is given by $\theta = \theta_0 \sin(2\pi ft)$. The maximum trailing edge excursion, denoted by A , represents a transverse length scale. We consider three pitching points - P1, P2, and P3 - at a distance $p = 0.125C, 0.3C$ and $0.48C$ respectively. A visual representation of these parameters is provided in figure 2. The pitching frequency spans from $0.25Hz$ to $8Hz$. However, surface water sloshing places a constraint on the upper limit of frequencies that can be explored

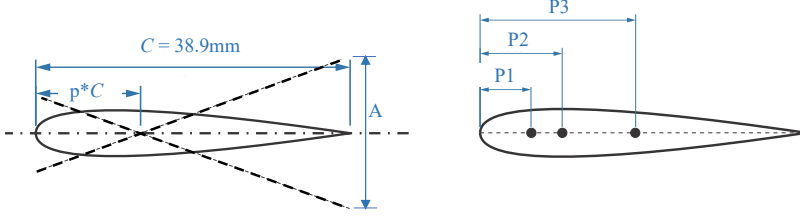


Figure 2: Illustration of the NACA0015 airfoil section with depictions of the trailing edge excursion on the left and the locations of pitching points on the right.

for each amplitude. We vary the amplitudes from approximately 5° to 20° . However, due to unsteady loading on the airfoil, the actual amplitude achieved from the spring mechanism exhibits a weak dependence on the oscillation frequency. Therefore, instead of using the exact values, we use the following notation to denote the amplitude set: A1($4.4^\circ - 4.9^\circ$), A2($9.1^\circ - 9.6^\circ$), A3($14.6^\circ - 15^\circ$), and A4($20.3^\circ - 20.7^\circ$). Nevertheless, the precise values of the trailing edge excursion, A , obtained directly from high-speed images of the airfoil cross-section in the self-propulsion state, are employed for calculating non-dimensional parameters.

We use an incremental magnetic rotary encoder (Reineshaw©LM10) with an angular resolution of 0.018° to measure the instantaneous position of the shaft. The linear resolution at the airfoil end is 0.3mm (approximately $0.007C$). The measurements are captured by a differential TTL module (NI9411) through the National Instruments©cDAQ 9174 data acquisition system at a sampling rate of 1kHz . The inset in figure 1 illustrates the instantaneous position of the airfoil with time for a representative case. The steady self-propelling state of the airfoil manifests as a linear region in the position-time curve. A linear function is fitted to the data within this region. The slope of this linear segment, averaged across 120 – 150 oscillation cycles (in 10 – 15 trials), is reported as the self-propelling speed U_s . The nature of the curve is similar for all the cases except for variations in the time taken to achieve self-propulsion and the slope of the linear region.

3. The self-propelling speed

In figure 3, we plot the self-propelling speed, U_s , as a function of frequency and amplitude for all three pitching points. To represent the range of variation and repeatability, error bars indicating twice the standard deviation are included in our plots for the measured self-propelling speed and the non-dimensional quantities derived from it. These error bars convey a 95% confidence interval for all reported values.

The self-propelling speed increases as the pitching point moves closer to the leading edge. As anticipated, U_s increases with frequency and amplitude for each pitching point (see figure 3). This increase is monotonic for all cases up to a frequency of 5Hz . For the higher amplitude pitching of A3 and A4, the self-propelling speed decreases with increasing frequency beyond 5Hz , except for P2-A3, which seems to plateau. These limiting frequencies for larger amplitudes also correspond to those where the airfoil actuation significantly deviates from sinusoidal pitching due to large normal forces. Interestingly, in the amplitude sequence A2, the speed exhibits a monotonic increase with frequency. This observation can be explained as follows: the normal force acting on the airfoil is anticipated to scale as $(fA)^2$. We observe a significant deviation from sinusoidal pitching at 5Hz when pitching at P2-A4 (figure 3). When pitching at a lower amplitude (like P2-A2), the normal forces of the same magnitude can be expected to occur at $\approx 10\text{Hz}$ since A2 is nearly half of A4. Therefore, we

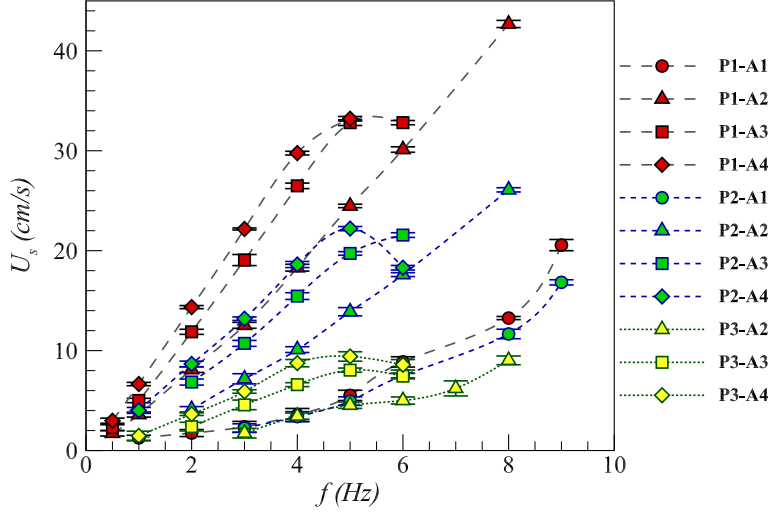


Figure 3: Measured self-propelling speed for different parameters is plotted with pitching frequency. P1, P2 and P3 correspond to different pitching points. A1, A2, A3 and A4 correspond to different amplitude of pitching.

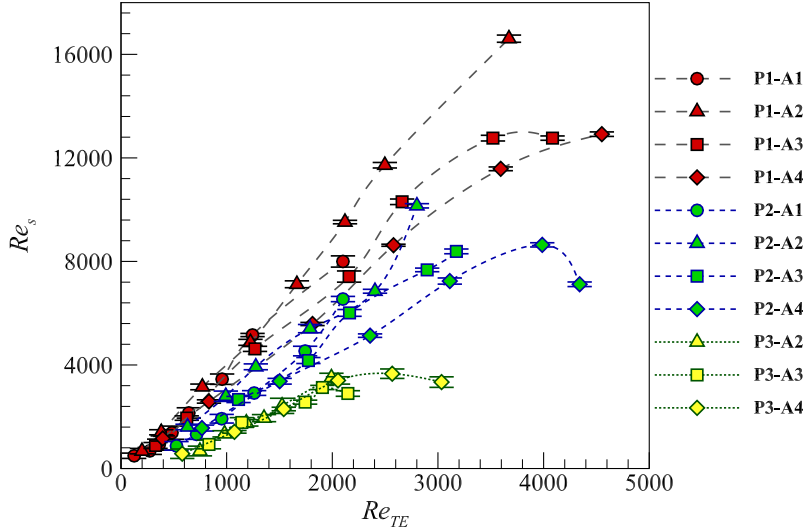


Figure 4: Self-propulsion Reynolds number Re_s is plotted against the trailing edge Reynolds number Re_{TE} across all the parameters studied.

anticipate that when pitching at A2, the plateauing frequency of U_s will exceed the range we have investigated..

While figure 3 provides a broad overview of the overall trend in self-propulsion, it lacks specificity regarding the dependence of U_s on input parameters. Notably, the self-propulsion speed exhibits a non-linear increase with frequency for low amplitude (A1) while maintaining linearity for other cases (A2-A3). Moreover, the exact relationship between amplitude and pitching point remains unclear.

Following [Gazzola et al. \(2014\)](#) and [Das et al. \(2016, 2022\)](#), the oscillation frequency (f)

and maximum trailing edge excursion (A), can be combined to establish a trailing edge velocity scale, U_{TE} . U_{TE} serves as a measure of the imposed kinematics and the velocity scale perpendicular to self-propulsion. This allows the definition of a trailing edge Reynolds number, $Re_{TE} = U_{TE}C/\nu$. Re_{TE} and Re_s are suitable parameters for capturing both length scales – normal excursion and longitudinal body length – and separating the input and output parameters. In figure 4, (Re_s) is plotted against Re_{TE} . Re_s values span two orders of magnitude, ranging from 400 to 17000, while Re_{TE} falls within the range of 100 to 4500 across all tested parameters. Re_s shows a linear increase with Re_{TE} when pitching at P3 for $Re_{TE} < 2400$. However, when pitching at P1 and P2, the relationship between Re_s and Re_{TE} exhibits a clear dependence on amplitude, highlighting that the effects of frequency and amplitude cannot be adequately captured by the velocity scale U_{TE} . Notably, for both P1 and P2, the largest Re_s values are observed when pitching at amplitude A2 for a given Re_{TE} . Moreover, the P1-A2 case demonstrates the highest rate of increase in Re_s with Re_{TE} . (Recall that P1= 0.125C, P2= 0.3C, P3= 0.48C, and A1 is 4.4° – 4.9°, A2 is 9.1° – 9.6°, A3 is 14.6° – 15°, and A4 is 20.3°- 20.7°).

Recognizing that the amplitude effect cannot be adequately captured by Re_{TE} alone, we adopt two different non-dimensional representations of the self-propelling speed: $U_{BL}^* = U_s/fC$, and $U_{AL}^* = U_s/fA$. U_{BL}^* represents the speed in terms of body lengths per oscillation; a commonly used non-dimensional parameter to compare the swimming speed of different fishes (Videler 1993). By excluding explicit dependencies on the trailing edge excursion (A), U_{BL}^* enables a clearer investigation into the amplitude dependence of self-propelling airfoils. By definition, U_{BL}^* is related to the inverse of the self-propelling reduced frequency k_s such that $U_{BL}^* = \pi k_s$. U_{AL}^* represents the speed in terms of lateral trailing edge displacement per oscillation and is equal to the inverse of the Strouhal number, St i.e., $U_{AL}^* = 1/St$. It also represents the ratio of the longitudinal distance travelled by the airfoil to the lateral distance traversed by the trailing edge. Unlike the conventional usage of k_s and St , which are inversely related to the speed, we prefer U_{BL}^* and U_{AL}^* for a more direct representation. However, the incorporation of k_s and St along with U_{BL}^* and U_{AL}^* aligns with the established usage of these parameters as standard in the oscillating airfoil studies.

Figures 5 and 6 illustrate the plots of U_{BL}^* and the self-propelling reduced frequency k_s against the normalized trailing edge excursion A/C . In figure 5, the data points for each pitching point are closely clustered, and U_{BL}^* increases as the pitching point approaches the leading edge. The maximum value of $U_{BL}^* \approx 2$ is noted when pitching closest to the leading edge (P1) at the highest amplitude A4. Generally, U_{BL}^* increases with the normalized trailing edge excursion A/C (and hence the pitching amplitude). However, for pitching points P1 and P2 and $A/C > 0.3$, the rate at which U_{BL}^* increases diminishes, indicating reduced sensitivity to further increase in amplitude. This diminishing effect of amplitude is more prominent in the k_s vs A/C plot (figure 6). Points corresponding to different frequencies cluster closely together for nearly the same A/C value when $A/C > 0.3$, indicating a linear dependence on frequency. The examination of steady-state swimming in oscillatory fishes from different species reveals that the normalized speed U_{BL}^* ranges between 0.2 and 0.8 (Videler 1993). Additionally, their tail-beat excursion typically falls within the range of 30 – 10% of their body length (Videler 1993) (corresponding to a tail-beat amplitude of 15% to 5%). Within this amplitude range ($0.1 < A/C < 0.3$), we observe that U_{BL}^* is within the range of approximately 0.2 to 1.2, with higher values particularly evident when pitching close to the leading edge (P1).

In figure 6, we observe a wide range of k_s values, from 1 to 22, indicating a considerable variation in the degree of unsteadiness across all examined parameters. Notably, for low-amplitude (A1) pitching, k_s values are remarkably high, ranging between 8 and 17. As the amplitude increases, k_s decreases following a $(A/C)^{-1/2}$ relationship (inset in figure 6).

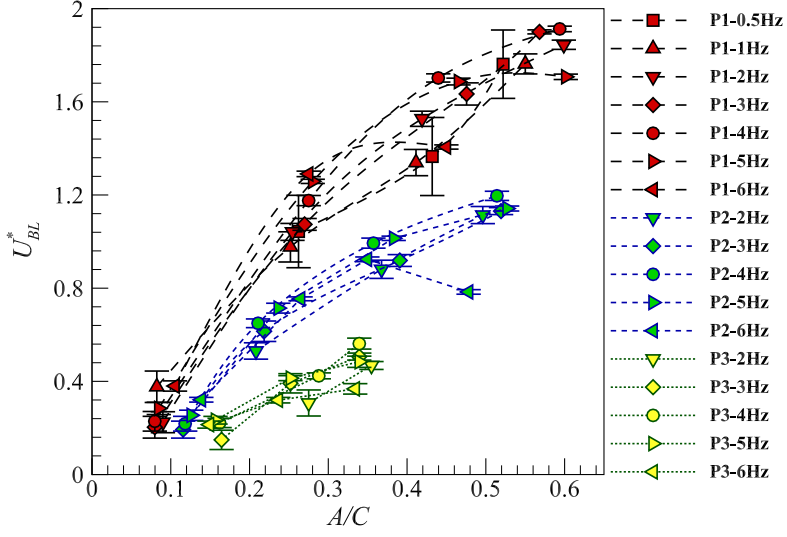


Figure 5: Variation of normalised speed represented as body-length per oscillation U_{BL}^* with normalised trailing edge excursion (A/C).

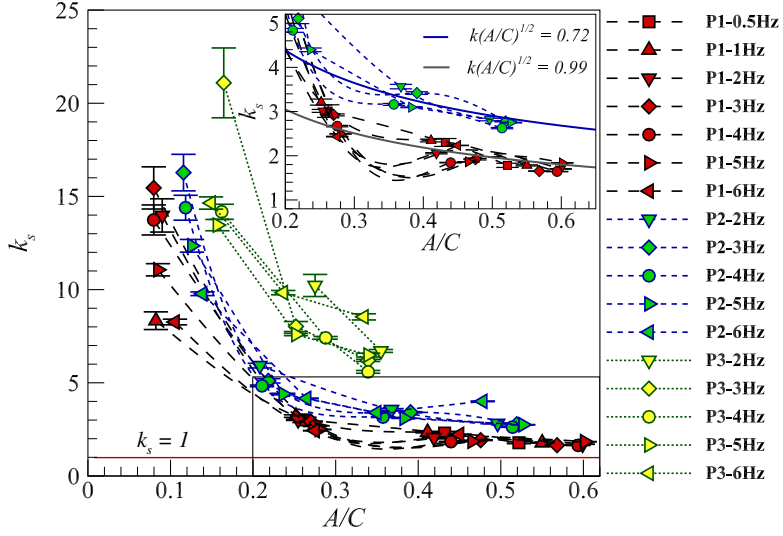


Figure 6: Self-propulsion reduced frequency k_s is plotted against the trailing edge excursion (A/C). The inset on the top right corner is the zoomed in plot showing the decrease in k_s as $(A/C)^{1/2}$.

Mackowski & Williamson (2015) observed k_s values in the range of 11 to 7 at the drag-thrust cross-over when pitching at 2° at a distance $0.25C$ from the leading edge. This comparison provides context for our study's observed k_s values.

Figures 7 and 8 illustrate the plots of U_{AL}^* and St with respect to Re_{TE} . As the airfoil is pitched closer to the leading edge, U_{AL}^* increases, and simultaneously, St decreases. When pitched near the center (P3), both U_{AL}^* and St exhibit values of the order of unity. The highest value of $U_{AL}^* \approx 4.8$ corresponds to pitching close to leading edge at $p = 0.125C$ (P1) with

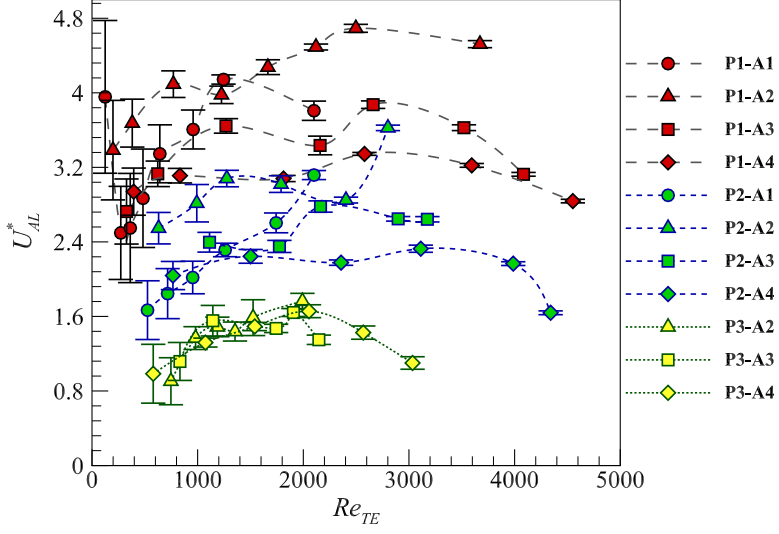


Figure 7: Normalised speed represented as the lateral trailing edge displacement per oscillation, U_{AL}^*

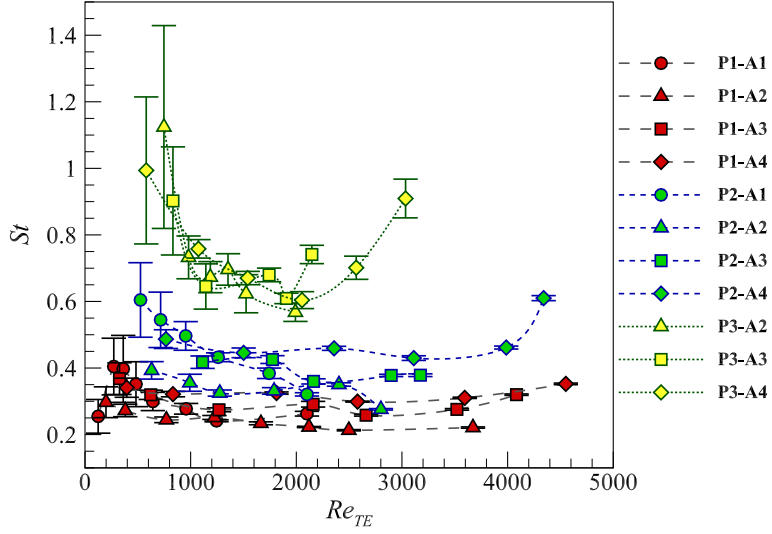


Figure 8: Strouhal number St across all the parameters studied.

amplitude A2 ($\approx 9.5^\circ$). Both U_{AL}^* and St values remain relatively constant for a given pitching amplitude, except for instances of lower Re_{TE} and when Re_{TE} exceeds 4500, but exhibit amplitude dependence. Specifically, for P1, the Strouhal number falls within the range of 0.2–0.4, aligning with the optimal range for thrust generation (Karniadakis & Triantafyllou 1989) while it exceeds this optimal range for other pitching points. A higher Strouhal number observed for other pitching points, implies a lower forward speed than the lateral velocity scale, perhaps leading to suboptimal and inefficient propulsion.

4. Scaling regimes

Following the observations and discussions in the previous section, we now focus on the distinct regimes that emerge based on imposed kinematics. Specifically, two different relations can be identified when pitching away from the centre (P1 and P2). At lower amplitudes (A1), self-propulsion speed exhibits a non-linear increase with frequency (see figure 3), leading to a *power scaling* regime. A scaling relation $Re_s \sim (1 - 2p)Re_{TE}^{3/2}$ based on a dynamic balance between inviscid thrust and enhanced skin friction drag emerges. At higher amplitudes (A2 - A4), a diminishing effect of the amplitude is observed, leading to a *separable scaling regime* (see figures 5 and 6). In this regime, $Re_s \sim (1 - 2p)^{1/2}Re_{TE}(A/C)^{-1/2}$ based on a balance between the inviscid thrust and a form drag. We validate the existence of these relationships through our experimental data. However, when pitching close to the centre, a linear relationship between Re_s and Re_{TE} becomes apparent, resulting in a *linear scaling regime* (see figure 4). For ensuring completeness, we also present these scaling relations in terms of non-dimensional speeds U_{BL}^* and U_{AL}^* .

4.1. Power scaling regime

When pitching at low amplitude (A1), we assume that the flow over the airfoil remains attached, and viscosity influences self-propulsion. In this regime, the impact of skin friction on self-propulsion is significant. The presence of a moving airfoil surface further enhances skin friction due to the thinning of the boundary layer in accordance with the Bone-Lighthill boundary layer thinning hypothesis (Lighthill 1971). While the boundary layer skin friction scales as $Re_s^{-1/2}$ for laminar unseparated flow over stationary boundary, it increases as $Re^{-1/2}|U_n|^{1/2}$ for moving surfaces (Ehrenstein *et al.* 2014), where U_n represents the normal velocity. For a pitching airfoil, $U_n \sim f\theta_0$ (Ehrenstein *et al.* 2014; Das *et al.* 2016). Consequently, the cycle-averaged drag coefficient $\overline{C_D}$ would scale as

$$\overline{C_D} \sim Re_s^{-1/2}(k_s\theta_0)^{1/2} \quad (4.1)$$

Through direct measurements of unsteady forces, Mackowski & Williamson (2015) established that the thrust generation on a pitching airfoil is primarily an inviscid phenomenon well captured by the linear inviscid theory of Theodorsen (1935) and Garrick (1936). In the limit $k_s \sim \infty$, the average thrust coefficient $\overline{C_T} \sim (1 - p)^2\theta_0^2k^2$, in line with the inertial thrust scaling adopted by Gazzola *et al.* (2014) and Das *et al.* (2016, 2019). Since $p < 1/2$, the leading order behavior of the thrust coefficient is given by

$$\overline{C_T} \sim (1 - 2p)k_s^2\theta_0^2 \quad (4.2)$$

In Appendix A, we establish that this inviscid thrust is primarily due to reactive forces, and the scaling relation Eq. 4.2 is valid for all $k_s > 1$.

In a self-propelling state, $\overline{C_D} = \overline{C_T}$. From Eq. 4.1 and Eq. 4.2 we get

$$Re_s^{-1/2} \sim (1 - 2p)k_s^{3/2}\theta_0^{3/2} \quad (4.3)$$

Noting that $k_s\theta_0 \sim Re_{TE}/Re_s$, the above scaling can be written in terms of self-propulsion and trailing edge Reynolds number as

$$Re_s \sim (1 - 2p)Re_{TE}^{3/2} \quad (4.4)$$

In figure 9, we compare our experimental data with the predicted scaling and find a close alignment when pitching away from the center (P1 and P2) and at low amplitude (A1) for $Re_{TE} < 2500$, the tested limit in this study.

Power-law relationship of the form with $Re_s \sim Re_{TE}^\alpha$ has also been reported by

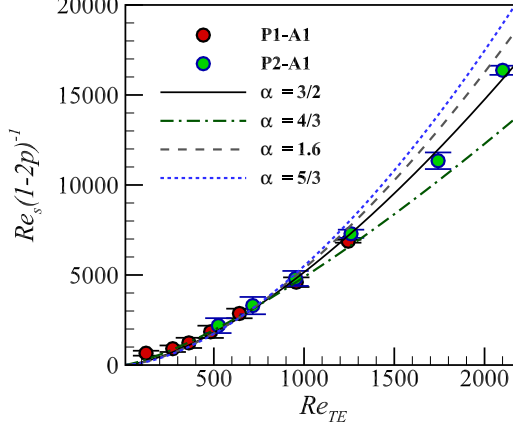


Figure 9: The *power scaling regime* identified for low amplitude pitching (A1) when pitching close to leading edge (P1 and P2). The symbols represent our experimental results while the curves represent the best fit for $Re_s(1-2p)^{-1} \sim Re_{TE}^\alpha$ with $\alpha = 3/2$ corresponding to the value derived in the present study (Eq.4.4) while $\alpha = 4/3, 1.6$ and $5/3$ correspond to the values reported by [Gazzola et al. \(2014\)](#); [Das et al. \(2016\)](#); [Lin et al. \(2021\)](#).

[Gazzola et al. \(2014\)](#); [Das et al. \(2016, 2022\)](#); [Lin et al. \(2021\)](#) where $\alpha = 4/3, 1.6$, and $5/3$ and $Re_{TE} < 2500, 2000$, and 400 , respectively. [Gazzola et al. \(2014\)](#) and [Das et al. \(2016\)](#) considered low amplitude oscillation (with $A/C \approx 0.2$ and 0.1 , respectively), while [Lin et al. \(2021\)](#) reported the scaling's validity for higher amplitudes too. Comparison with these predictions (figure 9) reveals that the difference between our study's derived scaling and that reported by [Gazzola et al. \(2014\)](#), [Das et al. \(2016\)](#) and, [Lin et al. \(2021\)](#) falls within the limit of experimental error upto $Re_{TE} < 1300$. However, the disparity between our scaling and that of [Gazzola et al. \(2014\)](#), particularly at higher Re_{TE} results from the difference in the assumed drag scaling. It's worth noting that neither of these earlier studies consider the effects of pitching point location, which is well captured by Eq. 4.4.

4.2. Separable scaling regime

When pitching at larger amplitudes (A2, A3 and A4), it is reasonable to assume that the primary hydrodynamic resistance is due to form drag ([Quinn et al. 2014](#); [Moored & Quinn 2019](#)). The pressure difference across the airfoil is expected to scale with the square of the self-propelling velocity such that $\Delta p \sim U_s^2$. This pressure force acts on a projected area proportional to the pitching amplitude θ_0 , resulting in a form drag coefficient $\overline{C_{D,form}} \sim \theta_0$. Considering a balance between the inviscid reactive thrust and form drag, we get

$$k_s \sim (1-2p)^{-1/2} \theta_0^{-1/2} \quad (4.5)$$

The above relation can be rewritten in terms of the Reynolds numbers as

$$Re_s \sim (1-2p)^{1/2} Re_{TE} (A/C)^{-1/2} \quad (4.6)$$

The compensated plot for Re_s in figure 10 shows an excellent experimental data collapse with the scaling (Eq. 4.6) applicable for $Re_{TE} < 4000$. We restate that for higher Re_{TE} , particularly at higher amplitudes such as A3 and A4, the airfoil encounters significant normal forces that cause it to deviate from pure pitching motion. This deviation plausibly explains the dip in the data points for $Re_{TE} > 4000$. The fitted line in figure 10 also shows a small

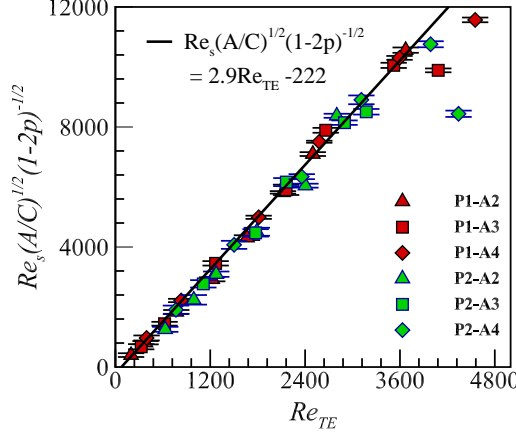


Figure 10: The compensated plot showing the *separable scaling regime* identified for higher amplitude pitching (A2-A4) when pitching close to leading edge (P1 and P2). The solid line represents the best fit for the data.

threshold value of $Re_{TE} \sim 35$ below which the airfoil does not propel. Nevertheless, Eq. 4.6 captures very well the linear dependence of self-propulsion speed on frequency and the diminishing effect of the amplitude. It's noteworthy that in the majority of fish species, which propel themselves through caudal fin oscillations, the forward speed is observed to increase linearly with the frequency of oscillation (Videler 1993).

While Lin *et al.* (2021) and Das *et al.* (2022) do explore higher amplitude pitching in their numerical simulations, neither study identifies a distinct separable scaling as observed in our experiments. Nevertheless, Das *et al.* (2022) reports a pronounced amplitude dependence in their power-law relationship when the pitching amplitude is greater than 8° . Recall that the smallest amplitude for which we observe separable scaling is $A2 \sim 9.5^\circ$.

4.3. Linear scaling regime

In figure 11, we re-plot Re_s versus Re_{TE} values, focusing on pitching close to the center at P3. The curve approximating the linear relationship is $Re_s = 2.1 Re_{TE} - 778$, with a threshold $Re_{TE,0} \approx 370$. When pitching close to the center, the contribution from reactive thrust becomes negligible. Based on inviscid theory (Garrick 1936), the dominant thrust contribution in this case is due to leading-edge suction (see Appendix A), which also scales as $k_s^2 \theta_0^2$. Considering large pitching amplitude (A2-A4), it is reasonable to assume that the form drag would be a dominant resistance. However, a balance between average thrust due to leading-edge suction and form drag $\overline{C_D} \sim \theta_0$ results in a relation very similar to separable scaling in Eq. 4.6. Importantly, this scaling argument fails to capture the observed linear behavior. In these cases, the flow around the airfoil is expected to be highly unsteady and complex, necessitating an in-depth analysis of instantaneous forces rather than average forces.

Vandenbergh *et al.* (2004) also reported a similar linear relationship for a heaving flat plate with $Re_{TE,0} = 480$ and slope $1/0.26$. For such a heaving flat plate and elliptical airfoils, self-propulsion is attributed to a bifurcation phenomenon characterized by symmetry breaking of shed vortices (Vandenbergh *et al.* 2004; Spagnolie *et al.* 2010). While it might be anticipated that pitching an airfoil at its center could lead to a similar symmetry-breaking phenomenon, we acknowledge the speculative nature of its possibility. Our current understanding is limited by a lack of insight into the instantaneous behaviour of the airfoil necessitating further

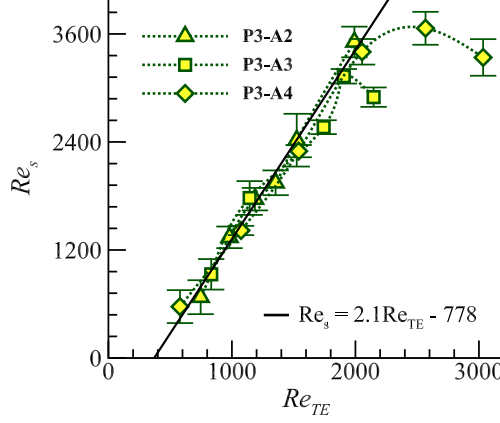


Figure 11: The compensated plot showing the *separable scaling regime* identified for higher amplitude pitching (A2-A4) when pitching close to leading edge (P1 and P2). The solid line represents the best fit for the data.

investigation. In any case, pitching at the center might not be effective from an application viewpoint, given that the airfoil's speed is the slowest in this configuration (refer to figure 3).

4.4. Scaling relations in terms of U_{BL}^* and U_{AL}^*

All the three scaling regimes can also be expressed in terms of U_{BL}^* and U_{AL}^* since they are related to Re_s and Re_{TE} as follows: $U_{BL}^* = Re_s(A/C)/Re_{TE}$ and $U_{AL}^* = Re_s/Re_{TE}$. We plot the scaling relations for U_{BL}^* in figure 12. For the low amplitude *power scaling regime*, $U_{BL}^* \sim (1 - 2p)Re_{TE}^{1/2}(A/C)$ and $U_{AL}^* \sim (1 - 2p)Re_{TE}^{1/2}$. In the separable scaling regime $U_{BL}^* \sim (1 - 2p)^{1/2}(A/C)^{1/2}$ and $U_{AL}^* \sim (1 - 2p)^{1/2}(A/C)^{-1/2}$. In the linear regime, we expect the normalized velocity U_{BL}^* to scale linearly with (A/C) beyond a threshold value of (A/C) . It is worth highlighting that viscosity dependence is observed exclusively in the low amplitude *power scaling regime* for both normalized speeds, whereas it remains independent in the other two regimes.

5. Concluding Remarks

In this study, we presented the self-propelling speed of a pitching NACA0015 airfoil across a range of imposed kinematics, encompassing variations in the pitching point location, amplitude, and pitching frequency. To directly achieve self-propulsion, we employed a rotary self-propelling apparatus. The reported self-propulsion values in our study demonstrate high repeatability, as evidenced by the presence of small error bars in most cases. However, it is essential to note that the limitations arising from surface water sloshing impose restrictions on the maximum Re_{TE} that can be investigated. Additionally, deviations in the anticipated trend at higher Re_{TE} are attributed to significant normal forces acting on the airfoil. This deviation is a consequence of the departure from sinusoidal pitching itself.

We presented the self-propulsion in terms of the non-dimensional parameters - self-propelling Reynolds number (Re_s), reduced frequency (k_s), and Strouhal number (St). We also introduced two normalized self-propelling speeds: $U_{BL}^* = U_s/fC$ and $U_{AL}^* = U_s/fA$. In general, the speed increases with an increase in both the frequency and amplitude of pitching. The highest speeds are observed when pitched closer to the leading edge. Specifically, the maximum normalized speed $U_{AL}^* \approx 4.8$, representing a forward body movement which

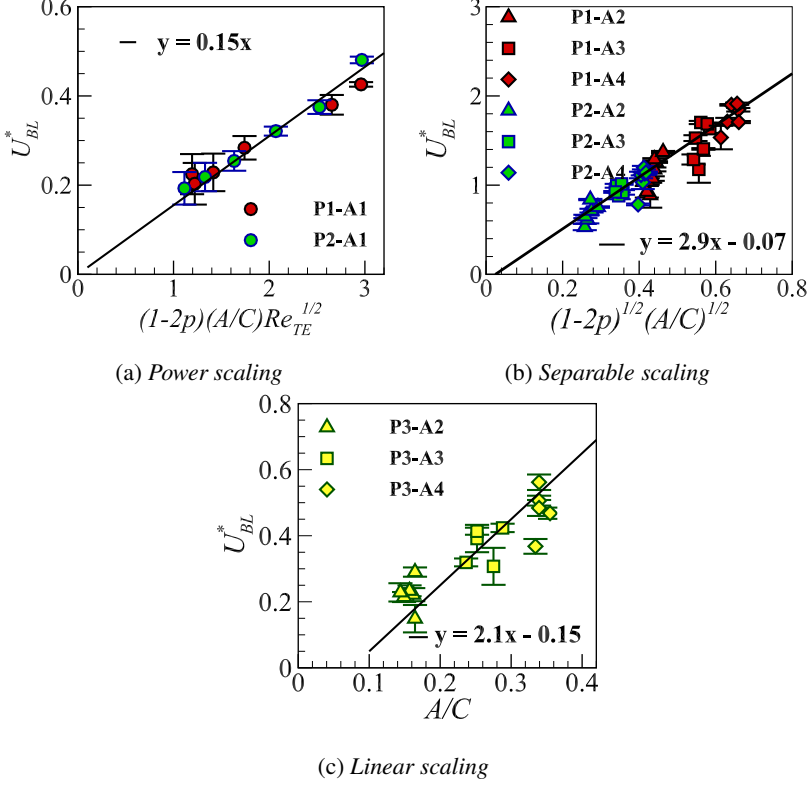


Figure 12: Scaling regimes represented in terms of normalised speed U_{BL}^*

is 4.8 times the trailing edge movement, is achieved for P1 (0.125C) and A2 ($\approx 9.5^\circ$). This corresponds to the lowest $St \approx 0.2$. On the other hand, the peak normalized speed $U_{BL}^* \approx 2$, corresponding to two body lengths per oscillation, is attained for P1(0.125C) and A4 ($\approx 20.3^\circ$).

The impact of imposed kinematics becomes evident through the existence of three distinct regimes of self-propulsion, each characterized by a unique relationship between Re_s and Re_{TE} . The three regimes reported in the present study are *power*, *separable*, and *linear* scaling regimes. The scaling regimes successfully capture and explain the non-linear increase in the speed at lower amplitude (A1) and the diminishing effect of the increase in amplitude for A2-A4 when pitching away from the center. Consequently, they highlight the importance of viscous skin friction in the *power scaling regime* and the dominance of form drag in *separable scaling regime*. We also identified an anomalous linear regime that does not follow from the balance of average forces like the other two. Furthermore, Re_{TE} as an integral parameter to assess the combined effect of frequency and amplitude was useful for low-amplitude pitching (P1-A1 and P2-A1) and when pitching at the center (P3, A2-A4). However, Re_{TE} proved inadequate in capturing the non-uniform dependence on frequency and amplitude when pitching at P1 and P2 at higher amplitudes A2-A3. In these instances, the speed increased linearly with frequency but followed a square root relationship with amplitude.

The present study lays the groundwork for advancements in understanding and optimizing the performance of self-propelling airfoils with significant implications for bio-inspired underwater vehicle design. We have specifically examined the kinematic or the 'speed'

aspect in exploring the self-propulsion in oscillating airfoils. Our present findings certainly provide sufficient insight into the question of how the self-propulsion speed is affected by the imposed kinematics. However, a crucial question of imposed kinematics' effect on efficiency remains unanswered. Moreover, present study focused on a cycle averaged (steady state) nature of self-propulsion while we pointed out the importance of understanding the unsteady dynamics, particularly when pitching at the center. Even in the context of the separable regime, very little is known about the point at which self-propulsion behaviour bifurcates from a non-linear power scaling to the separable scaling. Furthermore, observation of the separable scaling was limited to a maximum amplitude of $A_4 \approx 20^\circ$. A question here arises as to whether there exists an upper saturation limit in the amplitude that any further increase in amplitude does not increase the self-propulsion speed. Further research is essential to provide a satisfactory answer to these essential questions.

Acknowledgements. The authors acknowledge the discussions with Dr. Anil Das on the subject matter of this article.

Funding. This study was partially funded by the Naval Research Board. The first author received a subsistence fellowship provided by FERCC during the preparation of this manuscript.

Declaration of interests. The authors report no conflict of interest.

Data availability statement. The data that support the findings of this study can be shared on a reasonable request.

Author ORCIDs. Rakshita Joshi, <https://orcid.org/0000-0001-8831-8790>; Jaywant Arakeri <https://orcid.org/0009-0001-2575-0604>

Appendix A. Inviscid inertial thrust scaling

In the exploration of self-propulsion in oscillating airfoils, examining the theoretical foundation of the inviscid inertial thrust scaling is crucial. In sections 4.1 and 4.2, we derived the scaling relationships based on the premise that thrust generation is predominantly an inviscid mechanism established by Mackowski & Williamson (2015). For an airfoil pitching in a uniform free-stream, Das *et al.* (2022) further established that this inviscid thrust is primarily due to reactive forces on a purely pitching rigid airfoil in the asymptotic limit of reduced frequency $k \sim \infty$ where $k = \pi f C / U$, U being the free-stream velocity. Here we establish that this asymptotic relation holds even for lower values of k as long as $k > 1$.

A.1. Expressions for thrust coefficients

For an airfoil pitching sinusoidally in a uniform free-stream with angular velocity ω , the net thrust coefficient, C_T is given by

$$C_T = \langle C_T \rangle + C_{T,0} \sin(2\omega t - 2\phi) \quad (\text{A } 1)$$

Here, $\langle C_T \rangle$ is the average thrust coefficient, $C_{T,0}$ is the amplitude of oscillatory component of the thrust and ϕ is the phase lag with the respect to the pitching motion. The net inviscid propulsive thrust results from the linear superposition of reactive forces, the component of circulatory lift along the free-stream velocity, and leading-edge suction (Theodorsen 1935; Garrick 1936). Circulatory lift involves quasi-steady circulation due to a non-zero angle of attack and induced circulation caused by vorticity in the wake. $\langle C_T \rangle$ is then the sum of average reactive thrust coefficient, $\langle C_{T,R} \rangle$; circulatory thrust coefficient, $\langle C_{T,C} \rangle$; and leading-edge suction thrust coefficient, $\langle C_{T,LeS} \rangle$.

$$\langle C_T \rangle = \langle C_{T,R} \rangle + \langle C_{T,C} \rangle + \langle C_{T,LeS} \rangle \quad (\text{A } 2)$$

The expressions for thrust coefficients (average and unsteady components) due to different sources can be represented as functions of reduced frequency(k) and pitching point distance from the leading edge (p). Readers can refer to [Theodorsen \(1935\)](#); [Garrick \(1936\)](#) for detailed derivation. Following [Garrick \(1936\)](#), we get the following expressions for all the components and the total average thrust coefficients.

$$\langle C_{T,R} \rangle = \pi \theta_0^2 \frac{(1-2p)}{2} k^2 \quad (\text{A } 3)$$

$$\langle C_{T,C} \rangle = \pi \theta_0^2 \left(-F + k \left(\frac{3}{2} - 2p \right) G \right) \quad (\text{A } 4)$$

$$\langle C_{T,LeS} \rangle = \pi \theta_0^2 S_0 \quad (\text{A } 5)$$

$$\langle C_T \rangle = \pi \theta_0^2 \left(\frac{1-2p}{2} k^2 + T_0 \right) \quad (\text{A } 6)$$

Where,

$$S_0 = \left(F - k \left(\frac{3}{2} - 2p \right) G \right)^2 + \left(G + k \left(\frac{3}{2} - 2p \right) - \frac{k}{2} \right)^2$$

$$T_0 = -F + k \left(\frac{3}{2} - 2p \right) G + \left(F - k \left(\frac{3}{2} - 2p \right) G \right)^2 + \left(G + k \left(\frac{3}{2} - 2p \right) - \frac{k}{2} \right)^2$$

Here,

$$F = \frac{J_1(k) (J_1(k) + Y_0(k)) + Y_1(k) (Y_1(k) - J_0(k))}{(J_1(k) + Y_0(k))^2 + (Y_1(k) - J_0(k))^2}$$

$$G = -\frac{Y_1(k)Y_0(k) + J_1(k)J_0(k)}{(J_1(k) + Y_0(k))^2 + (Y_1(k) - J_0(k))^2}$$

$J_0(k)$, $J_1(k)$, $Y_0(k)$ and $Y_1(k)$ are the bessel functions of the first and the second kind respectively ([Bowman 2010](#)).

A.2. Asymptotic behaviour

We now examine the asymptotic behaviour of the average inviscid thrust coefficient, $\langle C_T \rangle$. In the limit $k \sim \infty$ ([Das et al. 2022](#)), the average thrust coefficient is such that

$$\langle C_T \rangle \sim (1-p)^2 \theta_0^2 k^2 \quad (\text{A } 7)$$

When pitching close to the leading edge, $p < 1/2$. Thus, the leading order behaviour of the average inviscid thrust coefficient is governed reactive thrust coefficient.

$$\langle C_T \rangle \sim (1-2p) \theta_0^2 k^2 \sim \overline{C_{T,R}} \quad (\text{A } 8)$$

In figure 13, we compare the relative contributions of reactive force, circulatory lift, and leading-edge suction to the total thrust for different pitching points considered in this study. We observe that the reactive thrust contribution alone accurately captures the overall trend of the inviscid thrust for both the average and oscillating components for P1 and P2. Furthermore, the asymptotic behaviour of the thrust coefficients in Eq. A 8 derived in the limit of $k \sim \infty$ is valid for $k > 1$. However, when pitching close to center, at P3, thrust generation is predominantly due to the leading edge suction. Therefore, the framework of linear theory allows the identification of the origins of thrust.

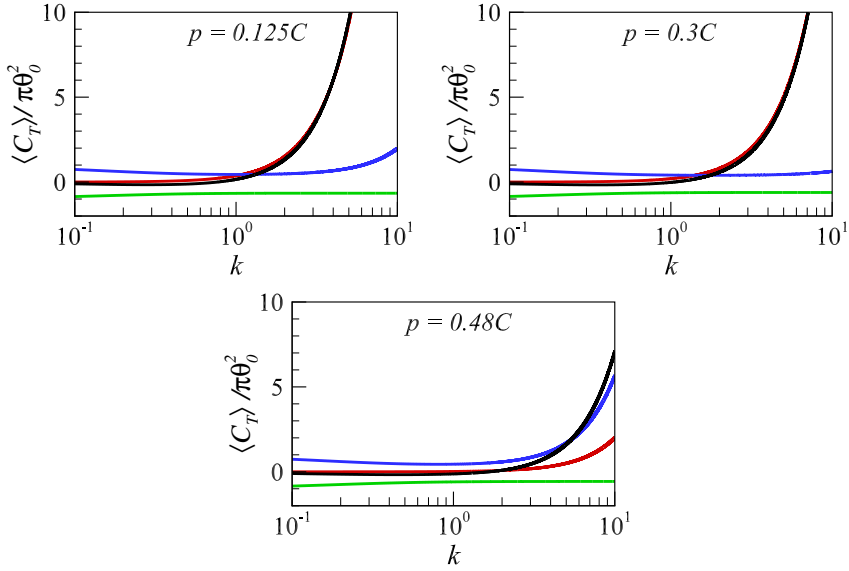


Figure 13: The components of the total average inviscid thrust coefficient (in black): reactive forces (in red), circulatory lift component (in green), and leading-edge suction (in blue). Refer to Eq. A 3, A 4, A 5, A 6 for the corresponding expressions.

REFERENCES

- ALBEN, SILAS & SHELLEY, MICHAEL 2005 Coherent locomotion as an attracting state for a free flapping body. *Proceedings of the National Academy of Sciences* **102** (32), 11163–11166.
- ALBEN, SILAS, WITT, CHARLES, BAKER, T. VERNON, ANDERSON, ERIK & LAUDER, GEORGE V. 2012 Dynamics of freely swimming flexible foils. *Physics of Fluids* **24** (5), 051901.
- BAINBRIDGE, RICHARD 1958 The Speed of Swimming of Fish as Related to Size and to the Frequency and Amplitude of the Tail Beat. *Journal of Experimental Biology* **35** (1), 109–133.
- BAINBRIDGE, RICHARD 1963 Caudal Fin and Body Movement in the Propulsion of Some Fish. *Journal of Experimental Biology* **40** (1), 23–56.
- BALE, RAHUL, HAO, MAX, BHALLA, AMNEET PAL SINGH, PATEL, NAMRATA & PATANKAR, NEELESH A. 2015 Gray's paradox: A fluid mechanical perspective. *Scientific Reports* **4** (1), 5904.
- BOWMAN, FRANK 2010 *Introduction to Bessel Functions*, first thus edn. Dover Publications.
- DAS, ANIL, SHUKLA, RATNESH K. & GOVARDHAN, RAGHURAMAN N. 2016 Existence of a sharp transition in the peak propulsive efficiency of a low- pitching foil. *Journal of Fluid Mechanics* **800**, 307–326.
- DAS, ANIL, SHUKLA, RATNESH K. & GOVARDHAN, RAGHURAMAN N. 2019 Foil locomotion through non-sinusoidal pitching motion. *Journal of Fluids and Structures* **89**, 191–202.
- DAS, ANIL, SHUKLA, RATNESH K. & GOVARDHAN, RAGHURAMAN N. 2022 Contrasting thrust generation mechanics and energetics of flapping foil locomotory states characterized by a unified - scaling. *Journal of Fluid Mechanics* **930**, A27.
- EHRENSTEIN, UWE, MARQUILLIE, MATTHIEU & ELOY, CHRISTOPHE 2014 Skin friction on a flapping plate in uniform flow. *Philosophical Transactions of the Royal Society A: Mathematical, Physical and Engineering Sciences* **372** (2020), 20130345.
- FISH, F.E. & LAUDER, G.V. 2006 PASSIVE AND ACTIVE FLOW CONTROL BY SWIMMING FISHES AND MAMMALS. *Annual Review of Fluid Mechanics* **38** (1), 193–224.
- GARRICK, I. E. 1936 Propulsion of a flapping and oscillating aerofoil. *Tech. Rep.* 567. NACA.
- GAZZOLA, MATTIA, ARGENTINA, MÉDÉRIC & MAHADEVAN, L. 2014 Scaling macroscopic aquatic locomotion. *Nature Physics* **10** (10), 758–761.
- GRAY, J. 1936 Studies in Animal Locomotion: VI Propulsive Powers of the Dolphin. *Journal of Experimental Biology* **13** (2), 192–199.
- GROSS, DAVID, ROUX, YANN, RAUFASTE, CHRISTOPHE & MÉDÉRIC, ARGENTINA 2021 Drag analysis with a self-propelled flexible swimmer. *Physical Review Fluids* **6** (5), 053101.

- JOSHI, RAKSHITA & ARAKERI, JAYWANT 2022 A Novel Experimental Apparatus for Studying Self-Propulsion. In *Fluid Mechanics and Fluid Power*, 2022. IIT Roorkee: Springer.
- JOSHI, RAKSHITA & ARAKERI, JAYWANT 2024 Long-distance sinusoidal actuation in self-propelling apparatus: a novel spiral spring-based crank rocker mechanism. *Sādhana* **49** (1), 16.
- KARNADAKIS, GEORGE EM & TRIANTAFYLLOU, GEORGE S. 1989 Frequency selection and asymptotic states in laminar wakes. *Journal of Fluid Mechanics* **199**, 441–469.
- LAGOPOULOS, N. S., WEYMOUTH, G. D. & GANAPATHISUBRAMANI, B. 2019 Universal scaling law in drag-to-thrust wake transition of flapping foils. *Journal of Fluid Mechanics* **872**, R1, arXiv:1903.03050 [physics].
- LAUDER, GEORGE V., ANDERSON, ERIK J., TANGORRA, JAMES & MADDEN, PETER G. A. 2007 Fish biorobotics: kinematics and hydrodynamics of self-propulsion. *Journal of Experimental Biology* **210** (16), 2767–2780.
- LIGHTHILL, MICHAEL JAMES 1971 Large-amplitude elongated-body theory of fish locomotion. *Proceedings of the Royal Society of London. Series B. Biological Sciences* **179** (1055), 125–138, publisher: Royal Society.
- LIN, XINGJIAN, WU, JIE & ZHANG, TONGWEI 2021 Self-directed propulsion of an unconstrained flapping swimmer at low Reynolds number: hydrodynamic behaviour and scaling laws. *Journal of Fluid Mechanics* **907**, R3.
- LIU, KUI, HUANG, HAIBO & LU, XI-YUN 2020 Hydrodynamic benefits of intermittent locomotion of a self-propelled flapping plate. *Physical Review E* **102** (5), 053106.
- LUCAS, KELSEY N., LAUDER, GEORGE V. & TYTELL, ERIC D. 2020 Airfoil-like mechanics generate thrust on the anterior body of swimming fishes. *Proceedings of the National Academy of Sciences* **117** (19), 10585–10592.
- MACKOWSKI, A. W. & WILLIAMSON, C. H. K. 2015 Direct measurement of thrust and efficiency of an airfoil undergoing pure pitching. *Journal of Fluid Mechanics* **765**, 524–543.
- MOORED, KEITH W. & QUINN, DANIEL B. 2019 Inviscid Scaling Laws of a Self-Propelled Pitching Airfoil. *AIAA Journal* **57** (9), 3686–3700.
- PANICCIA, DAMIANO, PADOVANI, LUCA, GRAZIANI, GIORGIO & PIVA, RENZO 2021 The performance of a flapping foil for a self-propelled fishlike body. *Scientific Reports* **11** (1), 22297.
- QUINN, DANIEL B., MOORED, KEITH W., DEWEY, PETER A. & SMITS, ALEXANDER J. 2014 Unsteady propulsion near a solid boundary. *Journal of Fluid Mechanics* **742**, 152–170.
- SHINDE, SACHIN Y. 2012 Creation of an Orderly Jet and Thrust Generation in Quiescent Fluid From an Oscillating Two-dimensional Flexible Foil. PhD thesis, Indian Institute of Science, Bangalore, India.
- SMITS, ALEXANDER J. 2019 Undulatory and oscillatory swimming. *Journal of Fluid Mechanics* **874**, P1.
- SPAGNOLIE, SAVERIO E., MORET, LIONEL, SHELLEY, MICHAEL J. & ZHANG, JUN 2010 Surprising behaviors in flapping locomotion with passive pitching. *Physics of Fluids* **22** (4), 041903.
- THEODORSEN, THEODORE 1935 General theory of aerodynamic stability. *Tech. Rep.* 496. NACA.
- THIRIA, BENJAMIN & GODOY-DIANA, RAMIRO 2010 How wing compliance drives the efficiency of self-propelled flapping flyers. *Physical Review E* **82** (1), 015303.
- TRIANATFYLLOU, MICHAEL S & BARRETT, DAVID S 1995 PROPULSION MECHANISM EMPLOYING FLAPPING FOILS.
- VANDENBERGHE, NICOLAS, ZHANG, JUN & CHILDRESS, STEPHEN 2004 Symmetry breaking leads to forward flapping flight. *Journal of Fluid Mechanics* **506**, 147–155.
- VIDELER, JOHN J. 1993 *Fish Swimming*. Dordrecht: Springer Netherlands.
- WANG, DOU, LIN, QINFENG, ZHOU, CHAO & WU, JIANGHAO 2022 Aerodynamic performance of a self-propelled airfoil with a non-zero angle of attack. *Physics of Fluids* **34** (3), 031901.
- WANG, WENJIANG, HUANG, HAIBO & LU, XI-YUN 2020 Optimal chordwise stiffness distribution for self-propelled heaving flexible plates. *Physics of Fluids* **32** (11), 111905.
- WU, BUCHEN, SHU, CHANG, WAN, MINPING, WANG, YAN & CHEN, SHIYI 2022 Hydrodynamic performance of an unconstrained flapping swimmer with flexible fin: A numerical study. *Physics of Fluids* **34** (1), 011901.
- WU, XIA, ZHANG, XIAOTAO, TIAN, XINLIANG, LI, XIN & LU, WENYUE 2020 A review on fluid dynamics of flapping foils. *Ocean Engineering* **195**, 106712.
- XING, JINGRU & YANG, LIANG 2023 Wave devouring propulsion: An overview of flapping foil propulsion technology. *Renewable and Sustainable Energy Reviews* **184**, 113589.
- ZHANG, JIE, LIU, NAN-SHENG & LU, XI-YUN 2010 Locomotion of a passively flapping flat plate. *Journal of Fluid Mechanics* **659**, 43–68.